Draft version November 14, 2024
Typeset using LaTeX default style in AASTeX631

Identifying Spicules in Mg II: Statistics and Comparisons with Hα

Vicki L. Herde [1,2] Souvik Bose [3,4,5,6] Phillip C. Chamberlin [1,2] Don Schmit [7] Adrian Daw [8] Vanessa Polito [3,9] and Gabriela Gonzalez [1,2]

[1] *University of Colorado Boulder, Boulder CO 80303*
[2] *Laboratory for Atmospheric and Space Physics, 3665 Discovery Dr, Boulder CO 80303*
[3] *Lockheed Martin Solar & Astrophysics Laboratory, Palo Alto, CA 94304, USA*
[4] *SETI Institute, 339 Bernardo Ave, Mountain View, CA 94043, USA*
[5] *Institute of Theoretical Astrophysics, University of Oslo, PO Box 1029, Blindern 0315, Oslo, Norway*
[6] *Rosseland Center for Solar Physics, University of Oslo, PO Box 1029, Blindern 0315, Oslo, Norway*
[7] *Cooperative Institute for Research in Environmental Sciences, 216 UCB Boulder, CO 80309*
[8] *Solar Physics Laboratory, NASA Goddard Spaceflight Center, 8800 Greenbelt Rd, Greenbelt, MD 20771*
[9] *Department of Physics, Oregon State University, 301 Weniger Hall, Corvallis, OR 97331*

ABSTRACT

The Sun's chromosphere is a critical region to understand when considering energy and mass deposition into the transition region and corona, but many of the smaller, faster events which transport a portion of this mass and energy are still difficult to observe, identify and model. Solar Spicules are small, spike-like events in the solar chromosphere that have the potential to transfer energy and mass to the transition region, but whose energetic origins are still being researched. Chromospheric spicule activity on-disk can be identified by observing temporary excursions in the red and blue wings of chromospheric emission lines. Researchers have demonstrated this in Hydrogen Alpha (Hα, 6563 Å), Ca II (8542 Å, k 3934 Å), Mg II (h 2803 Å, k 2796 Å), and Si IV (1394 Å, 1405 Å) spectral observations, with the vast majority of identification efforts focused on lower chromospheric observations of Hα and Ca II. Because any spicules which deposit mass and energy into the transition region must necessarily pass through the upper chromosphere, observations from this region such as Mg II or Hydrogen Lyman Alpha (Lyα 1216 Å) in enough quantity to perform proper statistics will be critical to fully characterizing spicules' impact on mass and energy transfer in the Sun. This research proposes a definition with numerical limits for how spicules appear in Mg II wavelengths, tunes an algorithm for automatically detecting spicules in Mg II spectral observations, and uses K Means Clustering to identify and display the full range of spicule spectrum shapes. This work will help allow statistical studies on spicules in the upper chromosphere to be as thorough as those of the lower chromosphere, allowing researchers to better understand the physical nature of spicules and their role in energy transfer and deposition in the solar atmosphere.

Vicki.Herde@LASP.Colorado.edu

bose@lmsal.com

Phil.Chamberlin@LASP.Colorado.edu

Donald.Schmit@Colorado.edu

Adrian.Daw@NASA.gov

Polito@lmsal.com

gabi.gonzalez@lasp.colorado.edu

Keywords: Spicules — Chromosphere, Quiet — Chromosphere, Active — Active Regions — Heating, Corona — Transition Region)

1. INTRODUCTION

The Sun's chromosphere is a region which is highly dynamic on all scales and has historically been difficult to study. This region changes from being plasma dominated ($\beta > 1$) with strong flows and convection re-arranging the magnetic field, to being magnetic field dominated ($\beta < 1$) where magnetic fields define structures, plasma volumes, and movements. In addition, all energy which heats the inexplicably-hot corona passes through this region to be deposited at its upper boundary in the transition region, where the majority of the temperature change takes place. Modeling the magnetic field is critical to understanding and predicting the trajectory for CMEs and the risks of SEPs and solar flares, while modeling plasma and energy movement are critical to understanding the source of coronal heating.

One current issue facing researchers is the inability to fully recreate solar spicules in modeling efforts. Spicules are fine, hair-like features on the Sun extending from the top of the photosphere up into the chromosphere, sometimes reaching as far as the solar transition region (TR). They are spikes of hot plasma enclosed within magnetic flux tubes which carry mass and energy up from the photosphere. We know that some spicules reach the TR to deposit their mass and energy while others do not, but we do not know how often this happens or how much mass and energy are deposited. A number of models have investigated spicule formation energy sources including Alfvén waves Cranmer & Woolsey (2015); Iijima & Yokoyama (2017), shocks and wave action Sterling et al. (2010); De Pontieu et al. (2004a), magnetic tension Martínez-Sykora et al. (2017), and magnetic reconnection Ding et al. (2011); Shelyag et al. (2018). Several groups have been studying spicule-like features in magnetohydrodynamic (MHD) models Martínez-Sykora et al. (2017); Chintzoglou et al. (2018); González-Avilés et al. (2020); Dover et al. (2020); Srivastava et al. (2023)

This includes two groups that have managed to simulate solar spicules in MHD models, but the drivers behind those efforts differ. Martínez-Sykora et al. (2017) found that including ambipolar diffusion created long, finger-like structures in the model results which seemed to agree with Lyα observations by Chintzoglou et al. (2018). On the other hand, Iijima & Yokoyama (2017) formed spicule-like structures in their model, concluding that Lorentz forces as opposed to heating drove spicule formation. Rapid time cadence upper chromospheric observations have the potential to differentiate between the models.

There have been many studies of on-disk solar spicules, but the vast majority focused on observations in the lower chromosphere with more than 45,000 identifications in Hα (6563 Å) and Ca II (8542 Å) (Hansteen et al. 2006; De Pontieu et al. 2007; Rouppe van der Voort et al. 2007; Langangen et al. 2008; Vourlidas et al. 2016; Rouppe van der Voort et al. 2009; Sekse et al. 2012, 2013b; Yurchyshyn et al. 2013; Rouppe van der Voort & de la Cruz Rodriguez 2013; Sekse et al. 2013a; Yurchyshyn et al. 2014; Rouppe van der Voort et al. 2015; Henriques et al. 2016; Shetye et al. 2016; Pereira et al. 2016; Lipartito et al. 2014; Skogsrud et al. 2016; Bose et al. 2019; Samanta et al. 2019; De Pontieu et al. 2009; Rutten et al. 2019; De Pontieu et al. 2011; Yurchyshyn et al. 2020; Sterling et al. 2020; Dover et al. 2020; Nived et al. 2022; Vilangot Nhalil et al. 2022; Chaurasiya et al. 2024; Bose et al. 2021a, 2019), while a few hundred spicules had been identified in upper chromospheric Mg II (2796.34 Å, 2803.52 Å) and Lyα (1215.67 Å) or TR Si IV (1403 Å) observations (Tian et al. 2014; Rouppe van der Voort et al. 2015; Skogsrud et al. 2016; Henriques et al. 2016; Bose et al. 2019; Narang et al. 2016; Chintzoglou et al. 2018, 2021; Vilangot Nhalil et al. 2022; Chaurasiya et al. 2024; Bose et al. 2023).

This has resulted in a relative lack of spicule examples in the upper chromosphere, a region which is critical to our understanding of how energy and mass are deposited into the TR. However, Herde et al. (2023) (hereafter referred to as Paper I) demonstrated the feasibility of a new untuned method for using Mg II observations from the Interface Region Imaging Spectrograph [IRIS] De Pontieu et al. (2014a) to identify a large number of on-disk upper-chromospheric spicule identifications for the purpose of statistical studies. This research builds on that paper by setting out the limits for how spicules appear in Mg II spectra, tuning the method, and applying it to a greater range of datasets. With access to large-scale Mg II spicule identifications, researchers can use this to understand how spicules evolve as they fade out of traditional Hα and Ca II observations and into hotter, higher emissions. This information would help close the observational gap between the lower chromosphere and the transition region, allowing for a more full understanding of solar spicules' energetic interactions with that boundary layer.

1.1. *Spicules*

Spicules are small, ubiquitous, jet-like features in the solar chromosphere which, when observed on the solar limb (edge), look like slender threads sticking out from the Sun's surface Roberts (1945). Physically, they are upflowing or downflowing streams of plasma constrained within small magnetic flux tubes above the Sun's surface. They were first identified on the solar limb by Italian priest and astronomer Angelo Secchi in 1871 Secchi (1871) and have since been matched to their disk-counterparts called Rapid Blueshift/Redshift Excursions (RBEs/RREs) Langangen et al. (2008); Rouppe van der Voort et al. (2009); Sekse et al. (2012). RREs and RBEs are so named because they appear to redshift or blueshift the spectral line wing for a short period of time.

Their importance in impacting the dynamics of the solar atmosphere has long been recognized (Beckers 1968, 1972) and they have formed a part of numerous reviews such as Beckers (1968, 1972), Roberts (1945), and more recently Tsiropoula et al. (2012). Spicules are found in both active and quiet regions on the Sun(Athay & Holzer 1982; De Pontieu et al. 2011), and estimates suggest that there are more than a million spicules on the Sun at any given time (Beckers 1972). Over the past 20 years, a great deal of detail has emerged on their spectral and general characteristics (e.g. De Pontieu et al. 2004a; De Pontieu et al. 2007; Rouppe van der Voort et al. 2009; Sekse et al. 2012; Yurchyshyn et al. 2013; Bose et al. 2019, 2021b; Bate et al. 2022; Bose et al. 2023), thanks primarily to the development of high resolution ground-based and space-based telescopes that achieve a spatial resolution better than $0.1''$. The interest in their study was massively revived after seeing-free, high-cadence observations were made possible by the Hinode spacecraft Tsuneta et al. (2008).

The original spicules observed (now called Type I, also referred to as dynamic fibrils or mottles) are longer in duration (3-5 min) and less energetic than their later-discovered counterparts. Dynamic fibrils appear primarily in active regions Pereira et al. (2012) while mottles are their quiet sun counterparts Rouppe van der Voort et al. (2007). Type I spicules receive energy from the leakage of photospheric oscillations (p-modes) which steepen into shocks in the chromosphere De Pontieu et al. (2004b); Hansteen et al. (2006). Later, in 2007, De Pontieu et al. (2007) discovered a new class of spicules called Type II. These spicules are shorter-lived (1-3 min), highly dynamic, and appear more often in regions of quiet Sun and coronal holes De Pontieu et al. (2007); Pereira et al. (2012). Unlike the Type-Is, the origin of Type II spicules is still debated, with magnetic reconnection Ding et al. (2011), non-linear propagation of Alfvénic waves Matsumoto & Shibata (2010) and release of amplified magnetic tension through ambipolar diffusion Martínez-Sykora et al. (2017) being the prime candidates.

As spicules evolve, their changing temperature shifts them into and out of different elemental spectral emission lines. Hα and Ca II emissions form lower in the chromosphere and at cooler temperatures while Mg II h 2803.52 Å and k 2796.34 Å emissions and Lyα 1215.67 Å form higher in the chromosphere and at higher temperatures Leenaarts et al. (2013). This means if a spicule is heated, it is first detectable in Hα and Ca II wavelengths, and may then switch into emitting at Mg II, Lyα, or even transition region Si IV wavelengths at high enough temperatures. This was discovered when Type II spicules were first identified and researchers noticed that they would appear to "fade" during their evolution. This rapid fading was correctly perceived as a sign of heating and/or opacity changes during their evolution, and was confirmed after the launch of the Interface Region Imaging Spectrograph (IRIS; De Pontieu et al. 2014b) mission, where the fading Ca II H spicules subsequently appeared in the hotter Mg II ultraviolet and sometimes Si IV passbands Pereira et al. (2014). Over the course of these studies, Type II spicules were sometimes found to be heated to TR Pereira et al. (2014); Rouppe van der Voort et al. (2015) and even coronal temperatures De Pontieu et al. (2011); Henriques et al. (2016); Samanta et al. (2019) and a study by (Samanta et al. 2019) found that most spicules observed in a quiet sun region appeared to transfer hot plasma into the corona, supporting similar observations of active regions De Pontieu et al. (2011); Ji et al. (2012). These properties make them a potential candidate that can contribute to the energy balance of the Sun's outer atmosphere.

Understanding spicule activity in the upper chromosphere, including how often lower-chromospheric spicules reach all the way through to the TR, is critical in being able to fully describe how spicules contribute mass and energy to the Sun's upper atmosphere and to modeling their associated magnetic field behavior. With the tools to easily identify thousands of spicules across multiple datasets, researchers will be able to better study upper-chromospheric activity for comparison with much better understood lower-chromospheric activity.

2. OBSERVATIONS AND DATA

2.1. *The Interface Region Imaging Spectrograph - IRIS*

This research primarily uses data from the IRIS instrument, which is a satellite-based UV slit spectrograph and imager that was launched in 2013. It records spectra in multiple bandpasses (133.2-135.8 nm and 139.2-135.8 nm at

0.04 nm resolution, 278.5-283.5 nm at 0.08 nm resolution) including around the Mg II emission line as well as co-spatial images in multiple wavelengths such as the 1400 Å Si IV bandpass. As a slit spectrograph, it can either observe one set of locations continuously in sit-and-stare mode, or can raster across an image collecting data in two spatial dimensions at the expense of temporal resolution De Pontieu et al. (2014a).

Observations included in this study span the range of solar environments, from quiescent sun to active region. Some datasets were also chosen for their co-observations with other observatories. The details for datasets used are listed in Table 1 We use both sit-and-stare mode and high-frequency raster mode because they provide a temporal cadence of less than 25 seconds, which allows us multiple observations of shorter-lived events. Of note, the 2014 and 2017 datasets were co-observed with SST.

Table 1. IRIS Mg II Datasets Used

Dataset	Type	Date	Time (UT)	Obs. Center	Raster FoV	Raster Cadence
Coronal Hole	large, dense, 4-step raster	24 Sept 2014	7:49:34	78", -167"	1.4"x174"	21.6 s
Active Region	very large, dense, 4-step raster	15 Jan 2015	05:06:15	191", -187"	167"x174"	22 s
Flare Watch	large, dense, 4-step raster	11 Nov 2015	13:59:14	-185", -235"	1.4"x119"	12.7 s
SST Coordination	Medium dense 8-step raster	25 May 2017	7:33:24	30",-89"	2"x62"	25 s
Decayed Network	sit-and-stare	14 Feb 2021	6:40:32	48", -376"	0.35"x119"	9.4 s

The presence of the Mn I and Fe I features near the Mg II k line wing at 2795.641 and 2795.829 Å could potentially interfere with this analysis as spicule signatures in the form of RBEs and RREs were first identified on-disk using the line wing. For this reason, we use the Mg II h (2803.52 Å) line to reduce fitting errors. Other studies have utilized the Mg II k line Rouppe van der Voort et al. (2015); Bose et al. (2019, 2021b,a); Chintzoglou et al. (2021); Chaurasiya et al. (2024).

2.2. *The Swedish Solar Telescope - SST*

This analysis incorporates the results from Bose et al. (2019, 2021b) in the form of a "mask" of spicule representative profile (RP) locations. Please refer to these papers for a detailed description of how these data were created.

The above masks were derived from Hα observations from the CRisp Imaging SpectroPolarimeter (CRISP)Scharmer et al. (2008) and Ca II K observations from the CHROMospheric Imaging Spectrometer (CHROMIS) on the Swedish Solar Telescope (SST)Scharmer et al. (2003). The observations were taken on 25 May 2017 with a 97 minute duration starting at 9:12 UT until 10:49 UT as part of a coordinated observation campaign with IRIS. The instruments observed an enhanced network region near disk center at heliocentric coordinates (45", -92"). They had a temporal cadence of 19.6s and a pixel scale of 0.037".

2.3. *Data Processing and Co-alignment*

The IRIS spectra were first processed by running them through a de-spiking procedure to remove cosmic ray hits. For comparison with SST data, the rasters were also trimmed to match the SST spatial and temporal coverage. The SST RP data were shrunk down to match IRIS resolutions and co-aligned for this analysis. These data were then each matched to the IRIS raster step closest in time, matching within 1.5 s. From there, each IRIS location co-located with a SST spicule RP was identified and its spectrum set aside for analysis.

3. METHODS

3.1. *Spicule Features in Mg II*

Spicules produce multiple unique signatures in various spectral lines which can be used for identification. Bose et al. (2021b) identified multiple of these signatures in the Hα line and designed an algorithm to automatically detect spicules in SST data. Similarly, Paper I demonstrated proof-of-concept algorithm to identify spicules which uses Mg II signatures as described by Rouppe van der Voort et al. (2015):

> RBEs and RREs can be readily identified as ... excursions of the central absorption feature k3 in the Mg II k [figure]. The shift of k3 leads to the enhancement of the wing so that the RBE/RREs appear as emission features far out in the wings. The line profile in [the figure] shows the RBE as a blue-shift of Mg II k3 and absence of a prominent k2v peak as compared to the average Mg II k profile.

Using the quote above, Paper I lists the primary identifiers of spicule spectra in Mg II to include a Doppler shift of the central absorption feature resulting in a difference between peak heights, an overall broadening of the base of the emission line, and an asymmetric brightening in the Mg II wing associated with the Doppler shift direction. These features are highlighted in Figure 1. Additional example profiles of on-disk Mg II spicules can be found in Bose et al. (2019, 2021b), and in Chintzoglou et al. (2021).

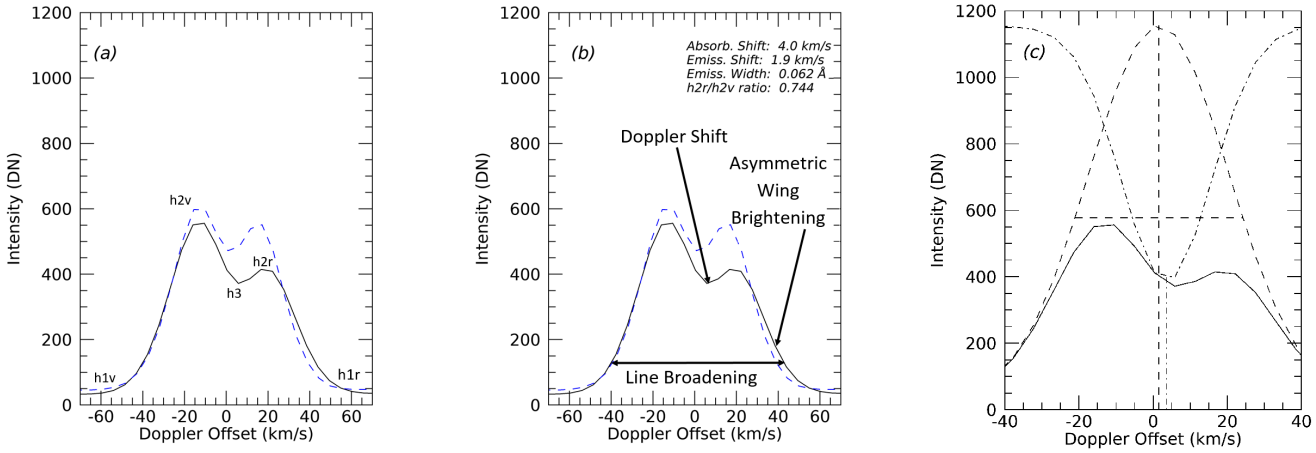

Figure 1. This figure taken directly from Paper I
Example of a redshifted spicule under the IRIS slit. Labels in (a) call out features in the Mg II line. (b) shows a redshifted spicule compared to a reference spectrum, where the solid line is the measured redshifted spicule spectral profile from IRIS. The dashed line is a reference spectrum, found by taking the mean of multiple datasets. (c) provides a visualization of how a Mg II spectrum can be modeled as the sum of a positive Gaussian plus a negative Gaussian. The negative Gaussian intensity values have been modified to highlight how they contribute to the central reversal.

3.2. *Selection Parameters*

In order to study spicule occurrences using Mg II, we must be able to clearly identify how spicules present themselves in these wavelengths and delineate boundaries for what does or does not count as a spicule. Rouppe van der Voort et al. (2015) provides a starting point for how to identify spicules, but we must translate those generalities into quantifiable measurements which are clear and repeatable.

Paper I identified four parameters which can be used in conjunction to identify spicule activity in the Mg II line. A Gaussian fitting method developed by Schmit et al. (2015) is used to approximate each spectrum as the sum of a positive emission Gaussian plus a negative absorption Gaussian, demonstrated in Figure 1(c). Note that the negative Gaussian values have been adjusted to highlight their contribution to the central line reversal. The Doppler shift of the absorption feature location is identified using the Doppler shift of the absorption Gaussian, which can provide its location even when one of the peaks is entirely suppressed. The location of the minimum value between the peaks was considered, but not used as many of the most extreme spicule spectra only have a single peak. The overall brightening of the base of the emission line was approximated using the width of the emission Gaussian. The asymmetric brightening in the wing was approximated using the Doppler shift of the emission Gaussian centroid, requiring that it be in the same direction as the Doppler shift of the overall line core. Finally we use the ratio between the h2v and h2r peaks to remove instances when the absorbing and emitting plasma are moving together as a bulk flow column. The ratio of the h2v and h2r line peaks is a standard indicator of Doppler-shifted plasma in the upper chromosphere Leenaarts et al. (2013). In the case of a large column of moving plasma, the entire Mg II line would be Doppler shifted and the ratio between the two peaks would remain relatively unchanged while in a spicule-like event, the ratio would shift.

It should be noted that due to the challenge of interpreting optically thick emissions, the Doppler shift and broadening of the emission Gaussian are simply fitting measurements and do not necessarily indicate a change in the plasma deeper in the atmosphere from which the Mg II line originates. Further study may explore these as diagnostics for that region, but such study is beyond the scope of this thesis.

From here, the method diverges from Paper I and turns to an analysis of co-aligned IRIS spectra and SST spicule locations in order to determine the appropriate cutoff values which define Mg II spicule spectra. To do so, we identify

all spectra in the IRIS data which are co-located with SST spicules in both space and time, and then calculate their Gaussian fitting parameters. Figure 2 shows histograms of the analysis parameters for these locations. The grey columns show the overall values, while the red and blue columns show the parameter distributions for these spectra which have red/blue shift agreement between emission Doppler shift, absorption Doppler shift, and peak ratio. Any spectrum which shows a redshift in one parameter but a blueshift in a different parameter is assumed to not be from a spicule. This is due to a second assumption that spicule spectra must show Doppler shift agreement in all parameters. Emission Broadening is not separated by Doppler shift direction. Using the above assumptions, the difference between the grey values and the red/blue values are from spectra which do not come from spicules. The data in Figure 2 have been smoothed with a 3-wide boxcar smoothing function to reduce noise.

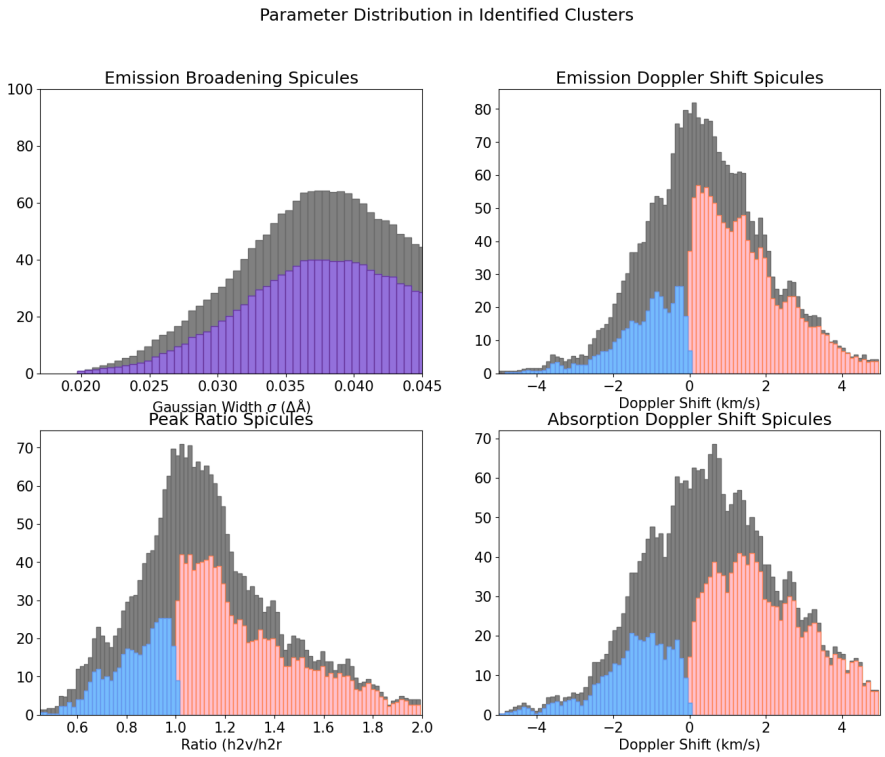

Figure 2. Histograms of non-normalized co-aligned spectra parameters. Grey data correspond to the parameter distribution over all IRIS locations co-aligned with SST Spicules. Red and blue data correspond to the subset of locations which show redshift or blueshift agreement between all three parameters. The difference between the grey and red/blue data corresponds to locations which display a redshift in at least one parameter and a blueshift in another.

While we expect a majority of these co-aligned spectra to be from Mg II spicules, many are not. There are several reasons for this. While any two observations may be in the same line of sight, SST and IRIS observe different altitudes in the solar atmosphere, with Ca II K forming lower in the atmosphere than Mg II h Bjørgen et al. (2018); Leenaarts et al. (2013). This spatial offset likely results in some number of spicules appearing in one observation but not the other. While each SST observation has a matched IRIS raster step within ± 1.5 s, any given IRIS observation may have as much as a 10 s difference between it and the closest SST observation. Since spicules have a lifetimes between 1-5 minutes and are also known to have fast sideways oscillations, a difference of 10 s can be significant for the most energetic events. Additionally, IRIS's lower resolution and 2x spatial and spectral binning introduces blending effects which impact observations. Finally SST must observe through the atmosphere, which introduces seeing effects that IRIS does not experience. As a result of these factors, we do not expect all spicules identified using SST to be visible to IRIS and vice versa.

Because spicules are by definition moving plasma and must have a Doppler shift, and because we expect the majority of these spectra to be from spicules due to their co-alignment with SST spicules, we expect to see a drop off in spectra near zero Doppler shift. Importantly, we also expect some percentage of co-aligned spectra to originate from non-

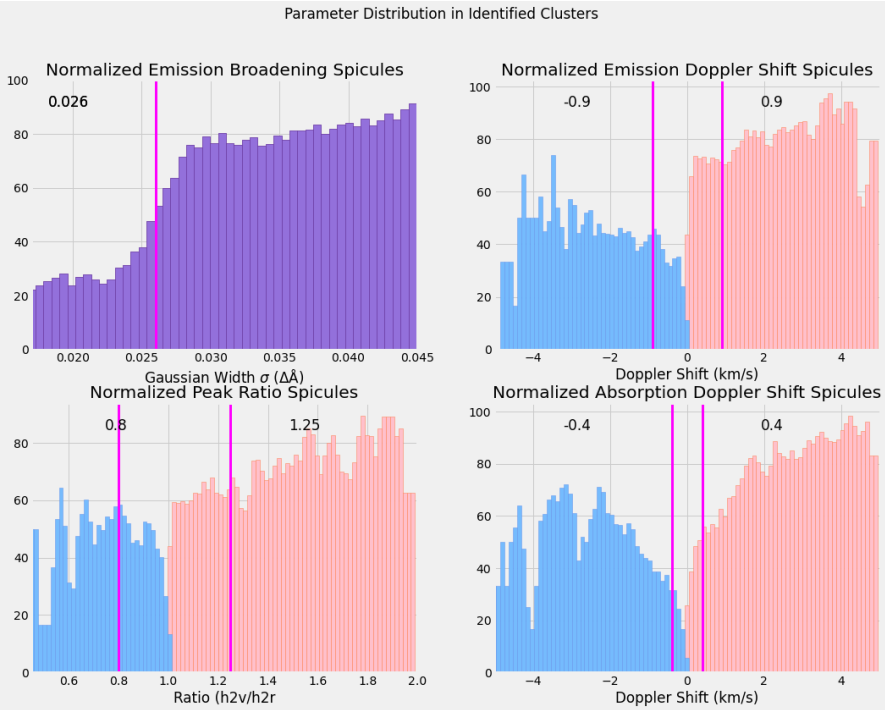

Figure 3. Histograms of normalized co-aligned spectra parameters. Similar to Figure 2, Red and blue data shows the subset of locations which show redshift or blueshift agreement between all three parameters. These parameters have been normalized by the overall histogram for each bin. Because Emission Broadening is independent of Doppler shift, purple values in (a) show the sum of redshifted and blueshifted locations, normalized by the total.

spicule features. While we do see sharp dropoffs as Doppler shifted parameters approach zero, some of this is influenced by overall trends in the dataset. Therefore, Figure 3 shows the same values from the previous plot, but normalized by overall values showing in grey. Because of its Doppler-free nature, the Emission Broadening values were normalized by the histogram for the overall dataset, and then scaled to range from 0 to 100. After normalizing, we look for strong dropoffs or drops and plateaus near zero Doppler shift.

From here, we define the cutoff for each parameter to either be where the parameter experiences a plateau or minimum near zero Doppler shift if there is a plateau, or the location of the fastest drop-off for histograms without a plateau. Emission Broadening, which doesn't have a Doppler shift, is determined by the fastest drop-off approaching zero. Any spectrum with one or more features within the cutoff bars we consider to not be of spicular origins, and any feature with an Emission Broadening below the cutoff bar is similarly considered to be not from a spicule. Sharp dropoffs within 3 pixels of the changeover between redshift and blueshift are data artifacts caused by the histogram binning. The results of this analysis can be found in Table 2. These cutoffs are purposefully strict to ensure that the identified events are actually spciules.

Identification Parameter	Cutoff Numbers. (Doppler shifts in km/s)
Absorption Doppler Shift	less than -0.4 or greater than 0.4
Emission Broadening	greater than 0.026
Emission Doppler Shift	less than -0.9 or greater than 0.9
Peak Ratio (Blue/Red)	less than 0.8 or greater than 1.25

Table 2. Cutoff Values Determined in Analysis from Paper 3

Paper 1 us a different method to determine parameter limits. Lacking confirmed spicule locations in a co-aligned dataset, limits were determined such that half of the values for each parameter would exceed the limits. To do so, the means and standard deviations for each parameter within each dataset were calculated. Then the average values between the three dataset means and standard deviations were found. This mean-of-means and mean-of-standard-

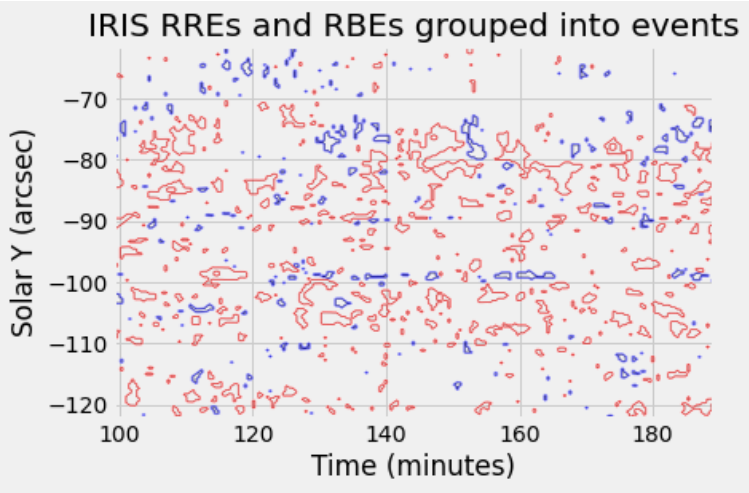

Figure 4. IRIS RREs (red) and RBEs (blue) at raster position 2 over time in the 2017 Plage dataset. Data are cropped to match the co-aligned SST observations.

deviations method was chosen to reduce bias because dataset sizes between different types of solar environments differed by over an order of magnitude. Limits were set at plus or minus 0.68 standard deviations from the mean. The number 0.68 was chosen as half the values of a Gaussian curve will fall within the mean plus or minus 0.68 standard deviations, while half will fall outside those values. This did not guarantee that half of the spectra would be identified as events, as a positive event identification is the result of a combination of all four parameters. Compared to the earlier analysis, later analysis shifted the all limits affected by Doppler shift blue-ward, combating the initial red bias introduced by IRIS's overall observed redshift. The most drastic change was to emission broadening, which was reduced by nearly half. As spicule identification results are highly sensitive to emission broadening, this change is responsible for most of the factor of 2-4 increase in decayed active network fill factor between Paper 1 and this work, as regions of low magnetic field values in particular had low emission broadening.

This method improves over past Mg II identification methods in its ability to identify spicule spectra automatically, with no additional manual input. This feature is key for middle chromospheric studies to be comparable to lower chromospheric studies. Without a thorough statistical understanding of spicule activity in the middle chromosphere, researchers will struggle to translate abundant lower-chromospheric observations into definite energetic depositions into the transition region.

3.3. *Event Grouping*

In order to understand spatial and temporal information about the identified events, we group pixels from neighboring regions in space and time. Many event regions appear to be connected but are separated by one pixel of non-event. We use the IDL function Morph Close to close these gaps, and then remove all events which have no neighbors in space or time, assuming them to be noise. We use the IDL function Label Region to identify and label each individual event. We then determine the duration of the event by taking the difference between the earliest and latest members of the group.

3.4. *K Means Clustering*

Prior to this analysis, there were few studies on the variety of shapes a spicule spectrum could take. Similar to Bose et al. (2021b), we use a machine learning technique called k means clustering to provide and display the variety of spicule shapes for reference in future studies.

K means clustering is a relatively simple machine learning technique to separate a dataset into similar groups of items, called clusters. For a set of x observations which each have d dimensions or attributes, we can sort them into k representative clusters. In this case, we used approximately $x = 2.5$ million spectra across our IRIS datasets. We consider each wavelength value to be a separate dimension, so our analysis which compares spectra between 280.29 nm and 280.42 nm analyzes $d = 50$ spectral bins or dimensions. The spectra will be sorted into k clusters, where k is chosen through methodical analysis.

To perform a k means clustering analysis, k random cluster centers (or representative profiles) each with d wavelength attributes are initiated. This analysis initiated them to have a starting distribution similar to that of our dataset, which reduces the number of iterations required before the analysis converges. From there, each spectrum is sorted into the cluster bin which is most similar, determined by summing over wavelength the absolute value of the difference between the spectrum and the cluster center. Once all spectra have been sorted into their most similar bin, the representative profile is recalculated to be the mean of all spectra within its bin for each wavelength. The sorting and update steps are repeated until no samples change bins, or until a certain number of iterations have been performed.

Technically k can be as large as the number of samples to be analyzed, but after a certain value, any analysis will provide decreasing returns. This value can be determined by performing the analysis over a range of ks and calculating the total variance between all observations and their assigned representative profile for each k. Plotting this, the optimal k will be located at the "elbow" of the data, showing where using a larger ks in the analysis provides decreasing impact.

This analysis compiled a list of all spectra in the datasets in Table 1 which were produced by spicules. The spectra were then analyzed using the k means clustering technique applied above, producing representative profiles. Representative profiles were then fitted according to the Gaussian fitting routine and compared against the spicule parameter limits to confirm consistency.

4. RESULTS

4.1. *Event Location Statistics*

This analysis identified a total of 13,347 spicules and nearly half a million spicule spectra in the associated IRIS datasets with a large variety of spectral shapes. Table 3 shows the number of spicules, the percentages of pixels (in space and time) marked as events, and the rate of events over time for all IRIS datasets.

Table 3. Spicule Location Statistics. Event rates are in $events\ arcsec^{-2}\ min^{-1}$

Dataset	Total RREs	Total RBEs	RRE Rate	RBE Rate	RRE Fill Factor	RBE Fill Factor
2014 Coronal Hole	3129	2440	0.071	0.056	8.0%	3.0%
2015 Flare Watch	731	256	0.093	0.032	8.1%	0.8%
2015 Active Region	652	579	0.060	0.053	5.0%	1.2%
2017 Plage	2704	2098	0.039	0.030	7.8%	1.9%
2021 Decayed Network	465	293	0.190	0.120	4.5%	1.4%

When identifying spicules in a plage region using Hα and Ca II K, Bose et al. (2021b) identified 19,643 RBEs and 14,650 RREs over the course of 97 minutes in a dataset that was roughly 54" by 50". This corresponds to a rate of 0.056 $RREs/min/arcsec^2$ and 0.075 $RBEs/min/arcsec^2$, and fill factors of 1.7% and 2.7% respectively. Analyzing the same dataset, we found 30% and 60% fewer events respectively, while finding spicule spectra at just over double the total area. Both 2015 datasets that also view active regions displayed higher RRE rates while similarly lower RBE rates. The decayed active network displayed the fewest spicules by pure events identified, but displayed a relatively high event rate compared to other datasets. This was the only sit-and-stare dataset analyzed and its relative lack of width compared to the size of a spicule likely affected the rate. When analyzing the fill factor, 2021 event rates returned to those of the other datasets.

When analyzing a quiet sun region displaying Type II spicules, Henriques et al. (2016) found a filling factor of 1% and 1.3% for RREs and RBEs using Hα, which is similar to our RBE rate in the decayed network, but only 22% our rate for RREs.

The higher fill factor but lower numbers compared to Bose et al. (2021b)'s observations has several potential explanations. It may be because spicules are multistranded and one "event" may be detecting multiple nearby spicules. Another factor could be that IRIS has a lower spatial resolution than SST. Because this analysis sets a requirement that detections have extent in either time or space, all single-pixel detections are removed. Bose et al. (2021b) does not apply this requirement and even if they did, SST's higher spatial resolution would set a smaller size minimum than IRIS. It's also possible that the spicules' orientation is causing them to appear larger in IRIS data as opposed to

SST, as spicules in the lower chromosphere may be more vertically oriented (and thus have a smaller apparent area) than those higher in the chromosphere. All these possibilities require additional direct comparison between IRIS and SST spectra to determine which might be true sources of differences between the observations.

In total we find slightly lower spicule rates compared to Hα observations in the co-aligned dataset, while similar or slightly higher rates in other active region datasets. We find much higher fill factors for both the active region and decayed network datasets compared to other Hα studies, particularly for RREs. The IRIS observations of the chromosphere show widespread overall redshift, and similarly we find a much higher rate of RREs over RBEs compared to analyses using Hα. It must be noted that this does not necessarily imply an overall downflowing volume of plasma, which might rule out spicules as a contributor to mass and energy in the chromosphere, since plasma flow is a function of velocity and density within events as well as number of events. Thus without additional detailed study of velocities and densities within spicular plasma as well as a better understanding of spicular activity in the upper chromosphere, we do not yet have the tools to fully determine their contribution.

In comparison to Paper 1, these results with updated parameter limits identify greater numbers of spicules in every dataset, primarily driven by the loosening of the emission broadening limit. The decayed active network saw the most gains, increasing in event numbers by factors of eight and four for RREs and RBEs respectively, while increasing in fill by factors of six and two. The Coronal Hole and Flare Watch datasets both saw an overall increase in event numbers on the order of two to five times, but their fill factors only moderately increased for RBEs by approximately 50% while RRE fill decreased by about 50%.

4.2. *Event Time Statistics*

IRIS raster rates generally ranged from 12-14 seconds, which defines the lower bounds for event duration. To qualify as an event and to remove spurious detections, events were required to have some extent in either time or space. Pixels which had no neighbors in either time or space were removed as noise, which eliminated most of the shortest-duration identifications.

Dataset	Median Event Duration	Mean Duration RRE	Mean Duration RBE	Median Duration RRE	Median Durati
2014 Coronal Hole	27	65±93	53±57	31	27
2015 Flare Watch	38	73±97	48±40	40	37
2015 Active Region	27	65±114	49±59	27	27
2017 Plage	49	90±120	67±60	49	49
2021 Decayed Network	28	49±66	34±35	28	27

Table 4. Spicule Time Statistics. All values are in seconds.

Event durations for our datasets can be found in Table 4. These durations are slightly longer than the median duration of 27.2 seconds identified by Bose et al. (2021b) but significantly shorter than those found in Paper 1 using a previous untuned version of this method. Bose et al. (2021b) also found that 98% of events had lifetimes shorter than 200 seconds. Other works (Rouppe van der Voort et al. 2009; Sekse et al. 2012; Pereira et al. 2012; Kuridze et al. 2016) found longer durations for RBEs and RREs ranging from 24 s to 400 s. Bose et al. (2021b) suggests that this may be because these works focused on single wavelength positions far in the blue or red wing of the Hα line profile. Overall, this analysis shows that identifying spicules using Mg II data can be done and results in similar detection rates and locations to co-aligned Hα observations.

4.3. *IRIS and SST Location Comparisons*

IRIS and SST show a both a great deal of overlap and a great deal of difference when comparing spicule locations using this method. Figure 5 shows IRIS and SST spicules at two different times. IRIS SJI 2796 Sii IV background images provide context, where active regions appear brighter and the vertical line at the center shows the leftmost raster location. Red (blue) contours outline SST RREs (RBEs), while pink (ice) contours outline IRIS RREs (RBEs). SST's field-of-view is rotated relative to IRIS's SJI, and thus appears to be diamond-shaped. IRIS's spicules are located in a tall rectangle just to the right of center. Only where these two fields of view overlap can their spicule locations be compared.

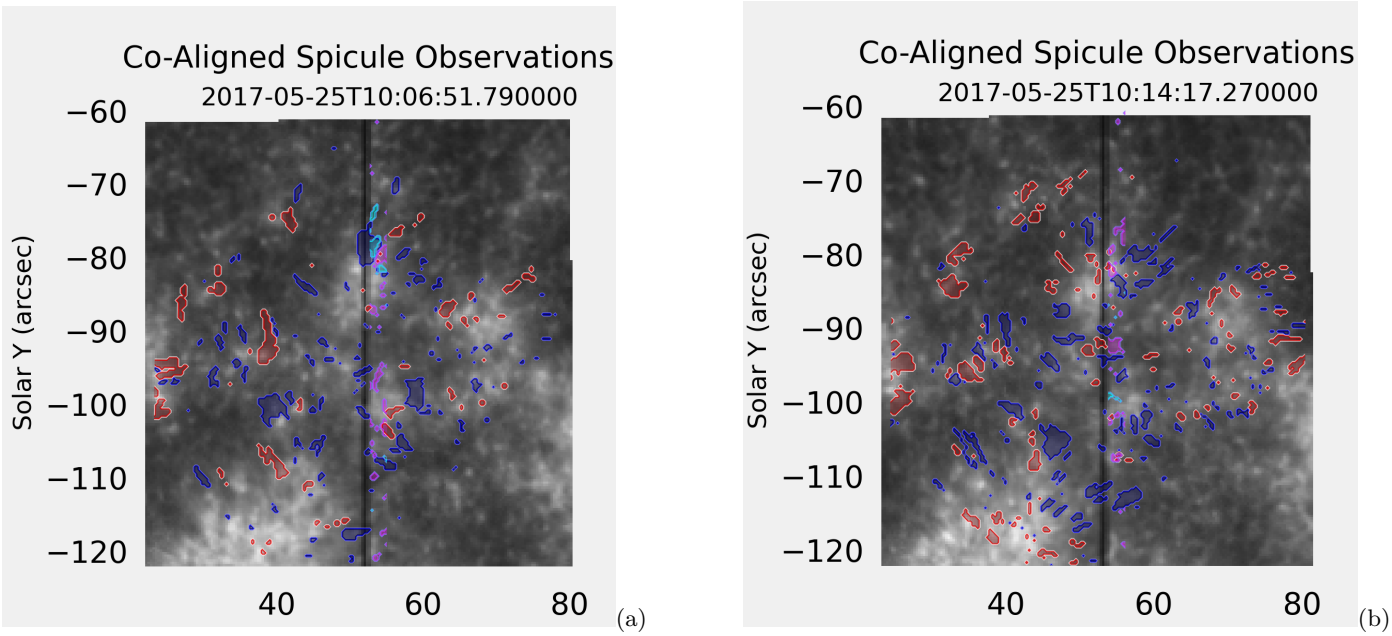

Figure 5. SST spicules and IRIS spicules plotted over an IRIS SJI 2796 Si IV image. SST RBEs (RREs) are shown in blue (red), while IRIS RBEs (RREs) are ice (pink). SST observations co-align in a diamond shape centered just to the left of the raster slit line, while IRIS raster observations co-align in a vertical strip centered just right of the slit line. Each background SJI image corresponds to the time when the raster slit was in its leftmost position at the start of its raster. Brighter areas in the background show active regions.

To compare the two spicule datasets, regions of red or blue spicules were grouped into events (considering both time and space). A hit mask was created to understand the agreement between the two instruments. For each SST spicule it was noted how many co-located IRIS pixels showed spicule spectra. Any event with at least one pixel of spicule overlap between the datasets was considered a hit. The results of this can be found in Table 5, which shows how often SST spicules overlap with IRIS spicules. Because a majority (63%) of SST spicules are small with total area $n \leq 3$ pixels (Figure 6), the table also shows the overlap percentage for only larger events.

Among All Events				
	IRIS RBE Overlap	IRIS RRE Overlap	RBE & RRE Overlap	No IRIS Overlap
SST RBEs	17%	6%	2%	79%
SST RREs	1%	57%	1%	42%
Among SST events with area n *pixels* > 3				
SST RBEs	36%	14%	7%	56%
SST RREs	3%	87%	2%	12%

Table 5. Percent of SST spicules which are overlapped by IRIS spicules for all events and for only events with area $n > 3$ pixels. RBE & RRE Overlap column is SSE locations which overlap with both an IRIS RBE and RRE. Rows do not add to 100 due to rounding and the intersection of the third column.

In the case of many larger events, there seems to be relatively high overlap, with the largest events showing similar shapes between observations. The smallest events (those with three or fewer pixels) rarely overlap. There are several explanations for areas of disagreement, particularly in smaller events. Because the two datasets observe slightly different times and locations, it is reasonable to assume that smaller events may be detectable by both instruments but the detections may offset from each other. Additionally due to temperatures or alignment, it may be the case that that some of these spicules in the lower chromosphere do not reach the middle or upper chromosphere. There may also be differences in observations due to seeing and instrument qualities. SST must contend with atmospheric effects while IRIS has a lower spatial resolution, both of which may affect which spicules are observed and identified. All of

these factors have a stronger impact on smaller events than larger events, which could explain why few of the smaller SST or IRIS events seem to overlap.

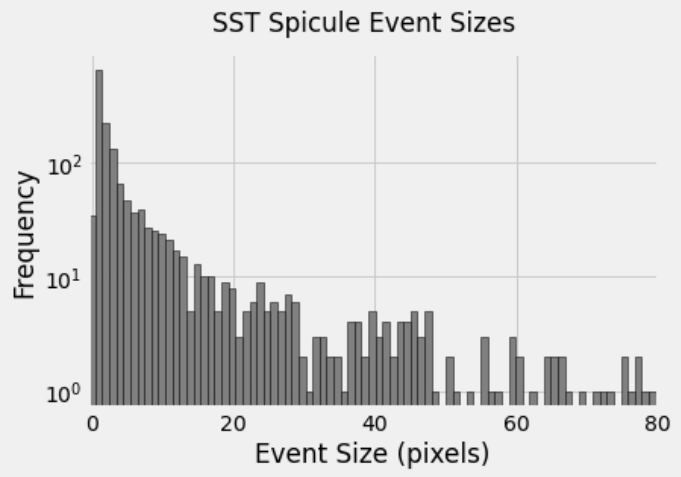

Figure 6. Histogram of SST spicules sizes in total number of pixels.

Among all events, SST RBEs were found to overlap with IRIS RBEs in 17% of events, decreasing to 6% overlap with IRIS RREs. SST RREs were co-located with IRIS RREs in 57% of events, decreasing to 1% overlap with their opposite Doppler shift. It is notable that SST agreement with IRIS is highest for redshifted events, likely due to the fact that IRIS found RRE areas at a rate of nearly 3.5 times more than that of RBE areas. SST events which overlap with both IRIS redshifted and blueshifted events are rare. These disagreements may be due to the repetitive nature of spicules or to detections of flux tube twisting. Type I spicules in particular tend to oscillate between redshift and blueshift at the same location over time, which may reverse during the time between SST and IRIS observations. In 2012, De Pontieu et al. identified contrasting Doppler signals in single events due to strong twisting motions in Type II Spicules in addition to flow-aligned Doppler signals.

4.4. *Examining Individual Events*

Looking closely at the images in Figure 5, we see several locations of overlap and several locations without overlap. For these images, the maximum difference between the SST image and the raster step is 25 seconds, which may be nearly half a Type II spicule's lifetime. Most images, however are within fifteen seconds of the raster data. In 5(a) at approximately $y = -77''$, we see a large SST RBE co-spatial with a medium IRIS RBE.

If we observe the preceding and following images in the associated video between timesteps 10:02:44 to 10:08:55, we see that both RBEs persist for approximately five minutes with the SST RBE growing from the bottom left to the top right until it intersects with the IRIS field of view.

Notice at the top of the two events, an IRIS RBE appears to jut out from an extension in the SST event. Its spectra are shown in Figure 7 while spectra from the rounded IRIS event just below it are shown in Figure 8. For each IRIS spectrum, a dashed scaled reference spectrum is provided for shape comparison. Spicule parameter values are located at the top right of each spectrum, with parameters exceeding spicule cutoff limits colored according to their Doppler shift. The spectra from the lower event have the h2v peak more strongly suppressed and a more strongly Doppler shifted absorption center, indicating that the lower event is moving faster than the upper event. A more thorough comparison of events at the spicule's boundaries in time or space will rely on a more detailed analysis of Hα spectra at those locations.

Figure 9 displays all IRIS spectra overlapping with the SST RBE at $x = 52''$, $y = -77''$ in Figure 5(a). Note this does not show all spectra from the adjacent IRIS RBEs in Figures 7 and 8. A review of fitting parameters shows that most events pass the emission broadening, absorption Doppler shift, and emission Doppler shift requirements, but do not pass the peak ratio requirement, with most ratios hovering between 0.9-1.0. Most of these locations are on the outer edges of the SST RBE. As mentioned in Section 3.2, a difference in peak ratio is indicative of a velocity differential between the lower and upper chromosphere Leenaarts et al. (2013). This event is one of the larger, longer-duration events identified by SST, lasting 5.5 minutes and covering 671 pixels.

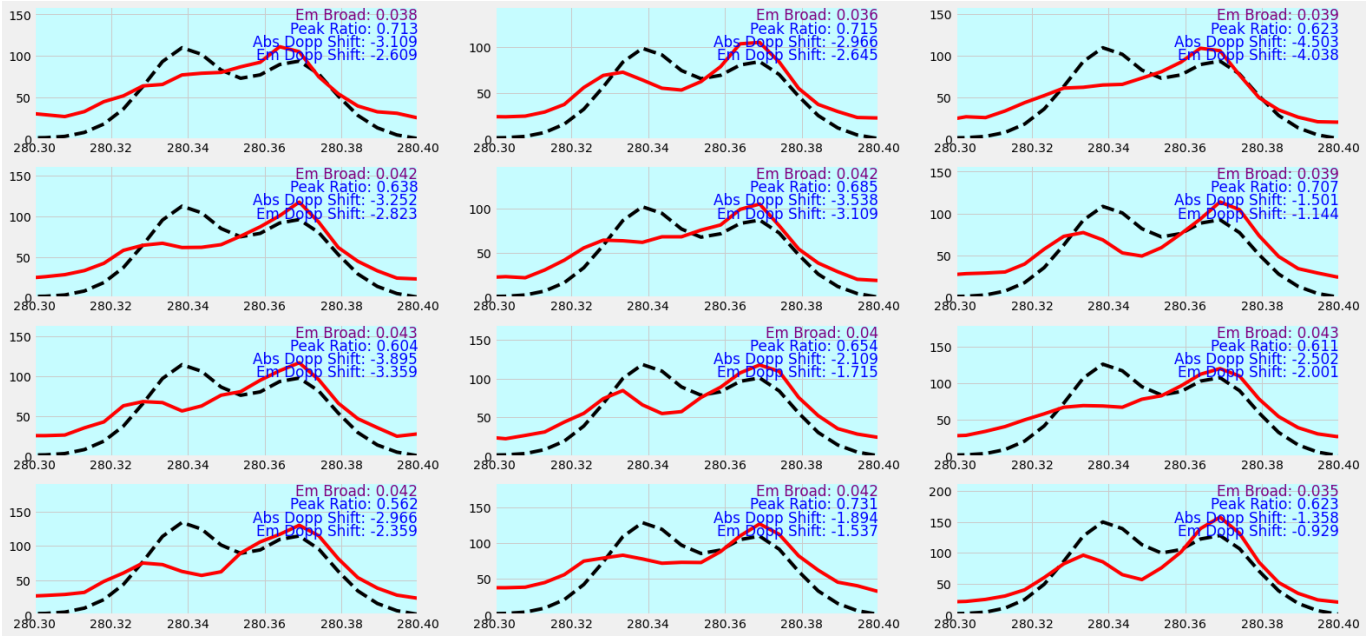

Figure 7. Spectra from the spike-like IRIS RBE at $x = 52''$, $y = -72''$ in Figure 5(a). Black dotted lines show an average reference spectrum, scaled to the level of the IRIS spectrum. Red lines are IRIS spectra. Fitted values for Emission Broadening, Peak Ratio, Absorption Doppler Shift, and Emission Doppler Shift are listed for each spectrum. Parameters which exceed the cutoff values in Table 2 are colored red, blue, or purple, as appropriate. Spectra which meet IRIS spicule requirements in all values have a red or blue background appropriate to their Doppler shift.

Looking at this RBE a different way, Figure 10 shows the spectrum from one of the pixels of the IRIS RBE, as well as a λ-Time plot showing that location's behavior over time. In the rightmost plot, blue lines indicate times which are RBEs while red lines are times which are RREs. The white marker indicates the time being examined. This image shows us that the location in question oscillates between RBE and RRE and back on a scale of approximately 10 minutes long. The strong central Doppler shift pattern suggests this may be a Type I spicule, which is supported by its longer duration of 5.5 minutes. Because of this spicule's presence in both Hα and Mg II observations, and because of the strong Doppler shift in the Mg II spectra, this event may be a good candidate for analysis to determine if it connects to and deposits its energy in the TR.

Examining a second event at $x = 54''$, $y = -103''$ from the same image, Figure 11 shows the IRIS spectra co-aligned with a SST Redshift event. In this case, all overlapping IRIS spectra are emitted by spicules. This RRE is also relatively long at 4.5 minutes and displays strongly Doppler shifted spectra, but has a lesser spatial extent than the previously examined RBE covering only 237 pixels. This event seems to bridge two unconnected, linear-shaped SST events between UTC 10:07 and 10:08 in the associated video, indicating that these two events may be connected, and both IRIS and SST spectra should be examined more closely to determine if this is true.

Figure 12 shows the λ-Time plot for a pixel at the center of this RRE. Its spectrum over time does not show the strong central Doppler shift pattern that the blueshift pixel shows, suggesting it may be from a Type II spicule. Its duration of 4.5 minutes indicates it is either not Type II, or more likely, is comprised of multiple events which are not individually distinguished by this method.

4.5. *Spicule Profiles*

Note: This section needs additional discussion.

Spicule spectra can have a wide variety of shapes, so we use a K-Means Clustering algorithm to provide a visual example of the range of shapes a spicule spectrum might take. A k of 40 was chosen by calculating the standard square error (SSE) for a range of k values and plotting them alongside with the difference between them (Figure 13). The SSE does not show a strong elbow, but the differential begins to flatten around $k = 40$, signifying that an increase in profiles beyond this point would not result in a significant increase in information.

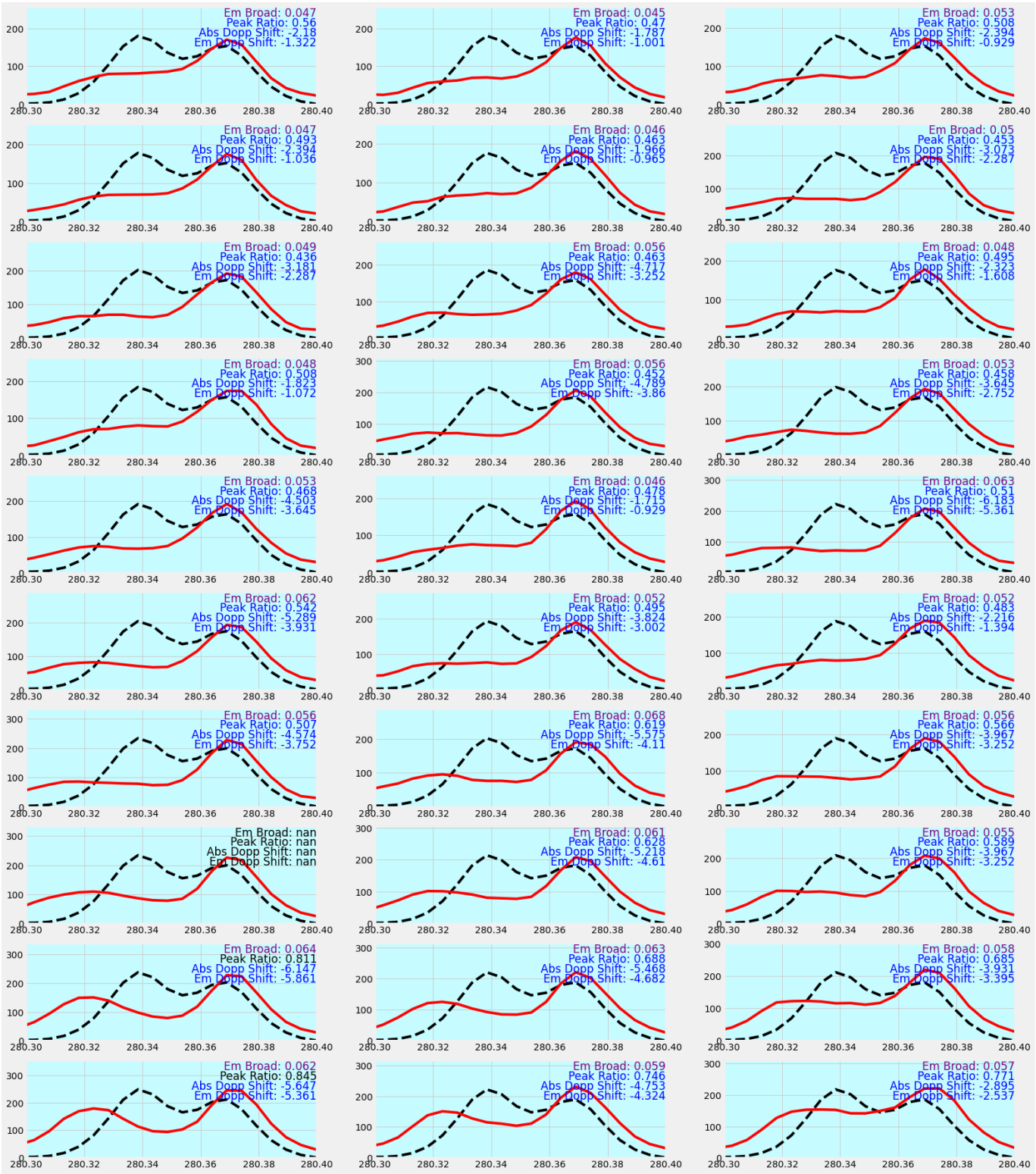

Figure 8. Spectra from the rounded IRIS RBE at $x = 52''$, $y = -77''$ in Figure 5(a). Figure is formatted similarly to 7.

Figure 14 shows the IRIS Mg II Representative Spicule Profiles (RPs), sorted by absorption feature Doppler shift. Normalized profile values are shown by the red line while a black reference spectrum is plotted for comparison. Each profile is highlighted according to whether it meets the parameter limits set out earlier. To the left of each spectrum

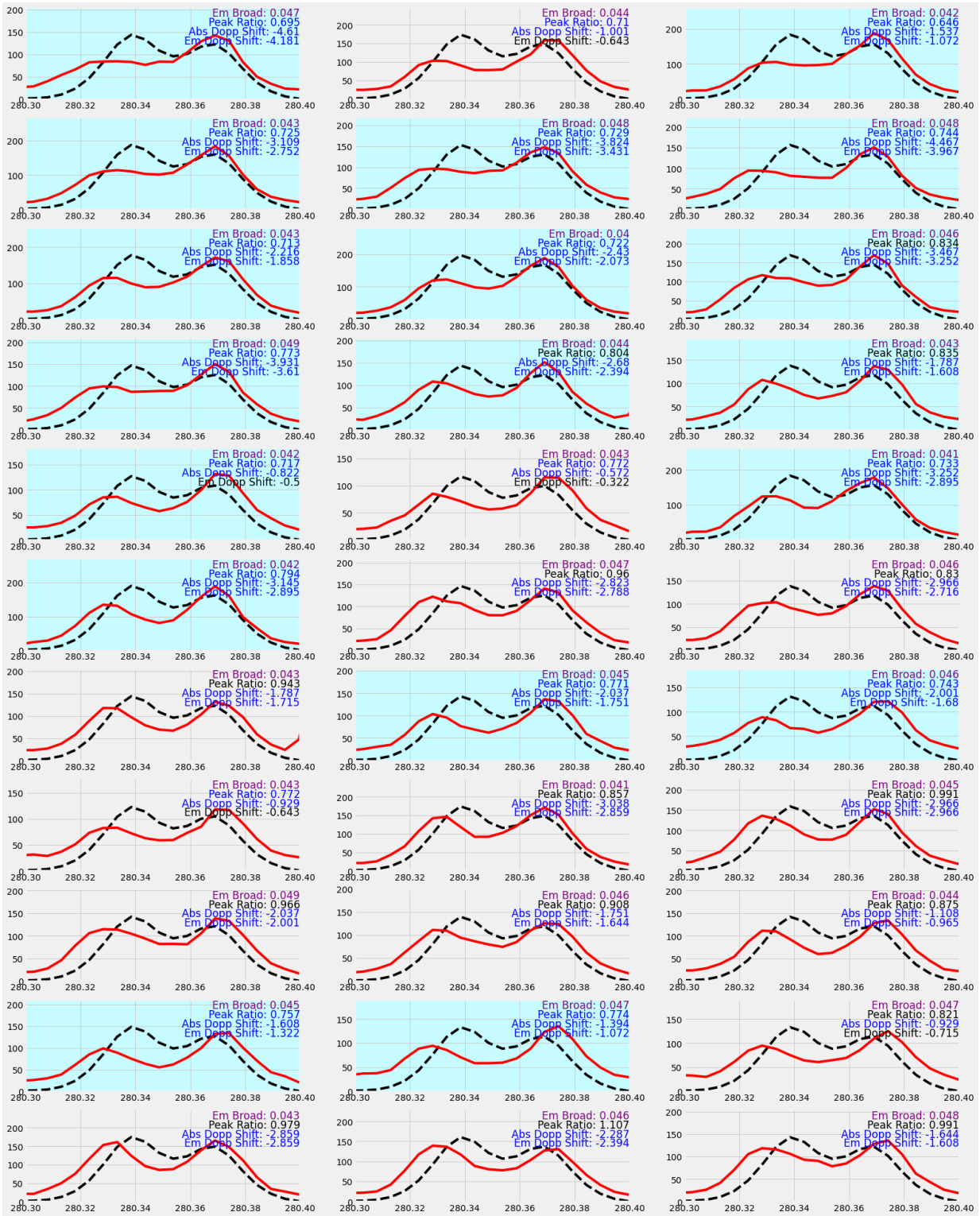

Figure 9. IRIS spectra which overlap with the SST RBE at $x = 52''$, $y = -75''$ in Figure 5(a). Figure is formatted similarly to 7.

is its cluster designation and the number of samples which contributed to its shape. To the right right of each profile are the associated fitting parameters. These profiles show the same preference towards redshift as the overall IRIS dataset does, which should not be taken to mean that blueshifted spicule spectra show less variety or range.

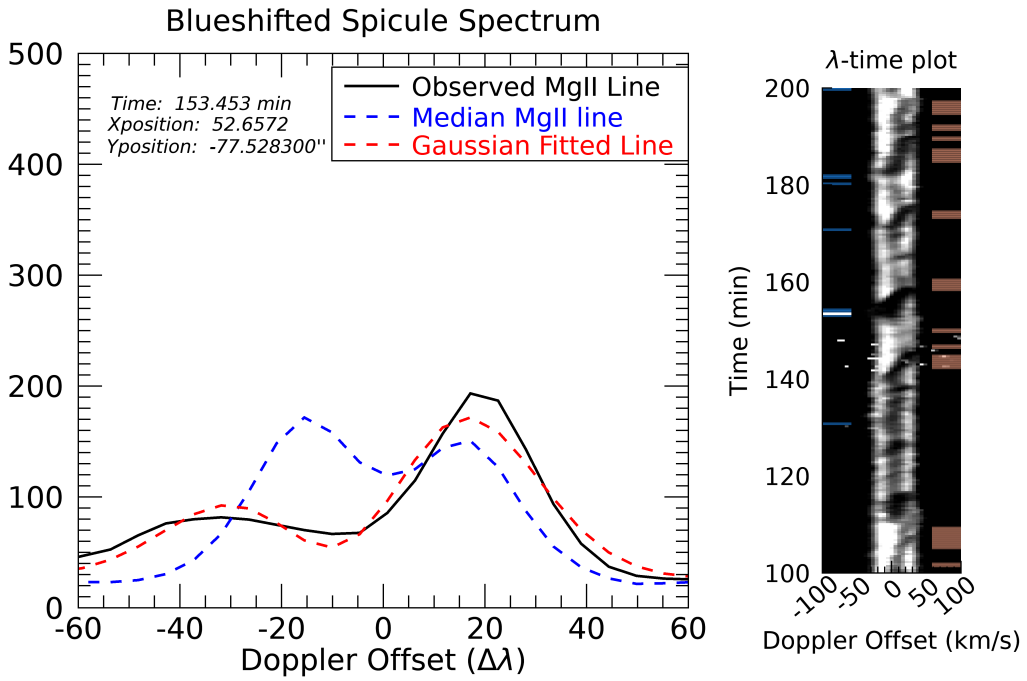

Figure 10. Examining an RBE location over time. The left plot shows the spectrum (black) of a spicule from the RBE at at $x = 52''$, $y = -77''$ in Figure 5(a), its modeled Gaussian fit (red dashed), and a median reference Mg II profile (blue dashed) with arbitrary intensity units. The spectrum's time and location are listed in the top left along with the Gaussian fit parameters used in this analysis. Subplot (b) shows that location's spectrum over time with the scale adjusted to highlight the central feature. Blue lines on the left indicate when the location is identified as a blueshifted spicule, and red lines on the right indicate redshifted spicule times. The white line corresponds to the profile from (a).

A total of 11 RBE profiles and 29 RRE profiles were identified by the algorithm, reflecting the overall bias in the IRIS dataset towards redshifted spectra. The RPs comprised of the more than 20 thousand spectra were #14, #18, and #22 while those with less than five thousand spectra were # 12, #27, and #40. RP #12 and #40 both had unusually broad emission Gaussians, a feature which is common among RPs with fewer constituent spectra. RP #27 had no unusual fitting parameters, but had low Mg II emission compared to overall background emission.

Once a researcher is familiar with spicule spectra potential candidates can often be identified by eye, but this requires a preexisting familiarity with spicule spectrum shapes. Prior to this research there were fewer than five examples of what a spicule might look like in a Mg II spectrum, showing only a small range of what how these spectra might appear. Figure 14 provides a broad range of spicule spectral profiles to fully demonstrate their variety. We provide this so that future researchers can train their eye while also training their code.

4.6. *Study Limitations*

While the spicule identifications between SST and IRIS showed strong overlap in RREs at 57% agreement which increases to 87% agreement for larger events, it also displays significant differences, with 66% of all SST events having no overlap with IRIS events. This is strongly related to the overall higher numbers of smaller events seen by SST as well as the overall tendency towards redshift displayed by the IRIS spectra.

There are several potential explanations for these differences. The first is simply that due to IRIS's lower spatial resolution than SST, some of the Mg II spectra from smaller events were combined with their neighboring non-spicule spectra, resulting in spectra with suppressed spicule indicators. In addition, IRIs's 25 second raster cadence meant that an SST spicule appearing just after the raster step passes would not be observed by IRIS for an additional 25 seconds, which is near the lower limit for spicule lifetimes. Spicules which are still brightening or fading are likely more difficult for IRIS to detect, due to the spicule signatures having lower intensity compared to their spatial and temporal neighbors.

This is compounded by the fact that this research purposefully set strict limits on spicule feature requirements to avoid identifying any non-spicule events. Loosening these requirements, particularly peak ratio and emission Doppler

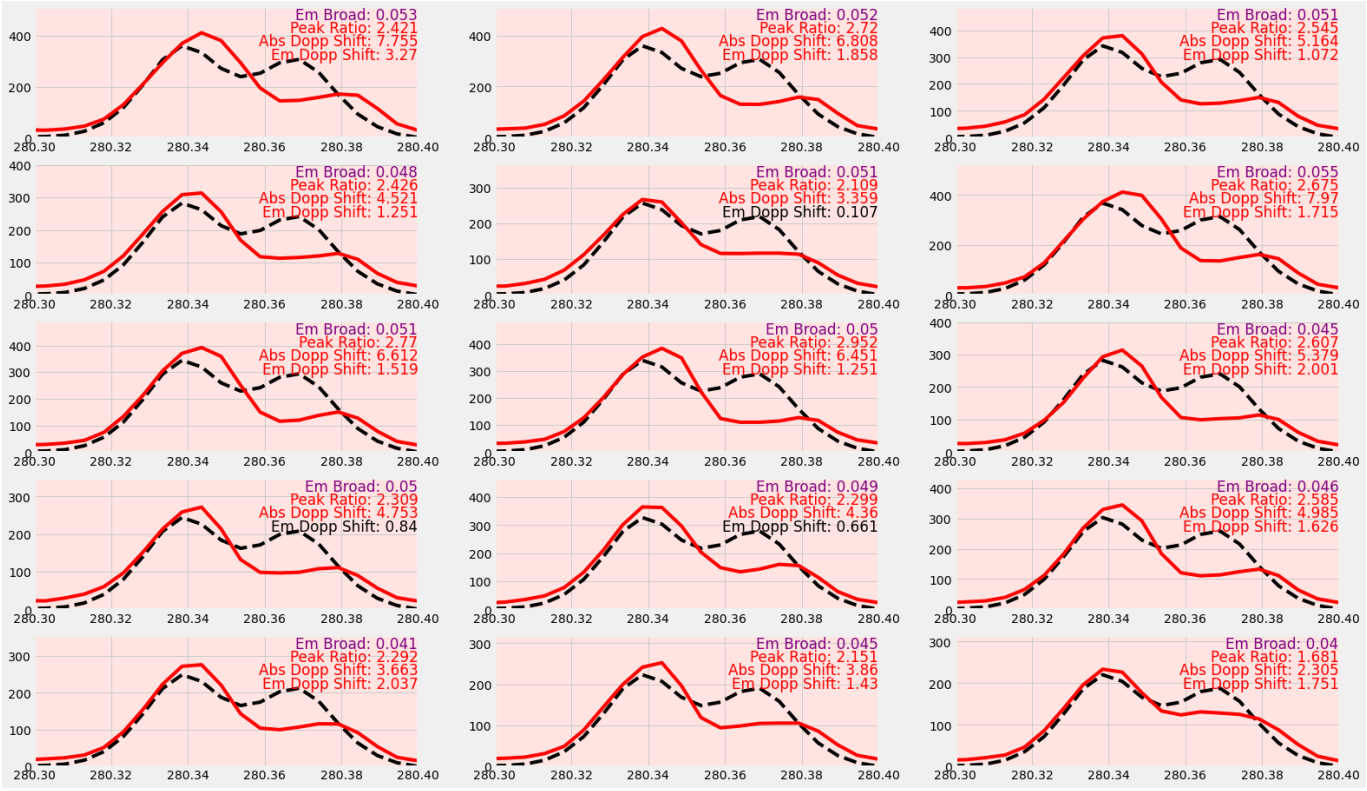

Figure 11. IRIS spectra which overlap with the SST RRE at $x = 54$, $y = -103$ in Figure 5(a). Figure is formatted similarly to 7.

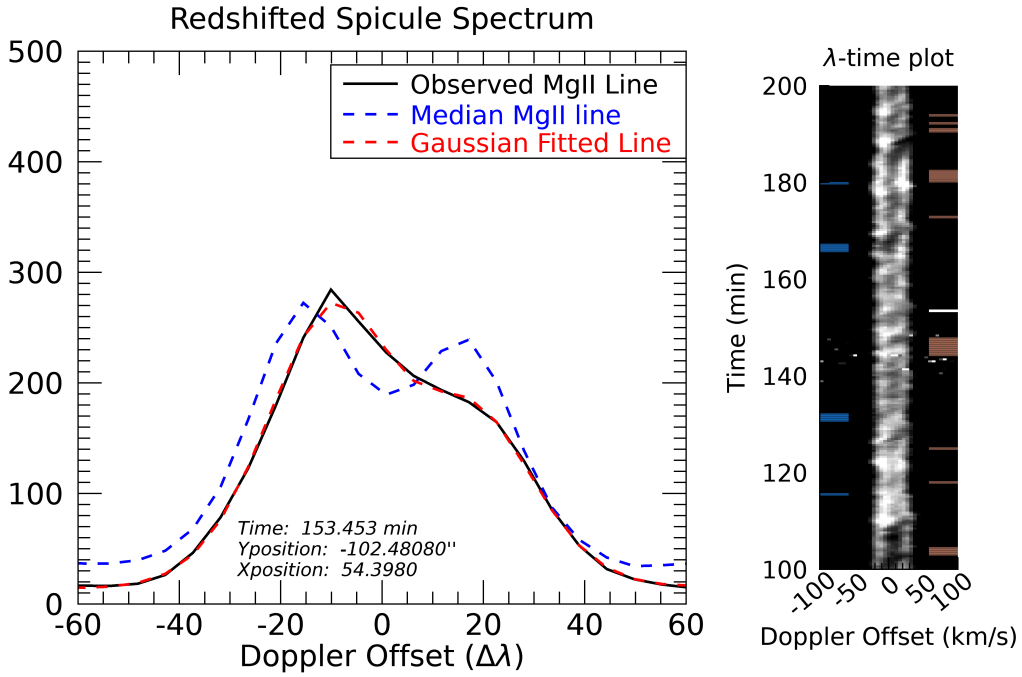

Figure 12. Examining a RRE location over time. Formatting identical to Figure 10.

shift, would increase the IRIS detection rate, particularly around the edges of already identified events. This would not, however address the overall bias towards redshifted events seen by IRIS. To do so, one would either need an IRIS

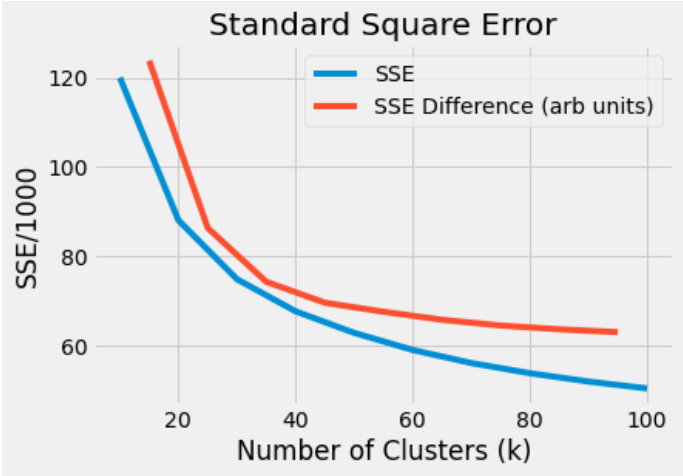

Figure 13. The standard square error (SSE) for a range of k values.

dataset which does not display an overall redshift of events, or asymmetric Doppler shift limits would be required. Asymmetric limits were considered, but were not implemented as the limits suggested by the histograms in Figure 3 were already relatively symmetric and as far as these authors are aware, no physical explanation has been proposed to support such asymmetries in spicule formation.

In addition, this work uses two different methods for spicule identification, which will impact the agreement between the two. The analysis by Bose et al. (2019) sorted spectra into representative profiles and then analyzed those profiles for spicule features. Because of this spectra which are on the boundary of being sorted into a non-spicule bin may actually not fully display the features which defined their RP as a spicule. A greater agreement between the two datasets can likely be reached by examining the IRIS and SST locations which differ and adjusting the K clusters or parameter limits accordingly. However, that analysis is outside the scope of this research.

To further examine an SST event which does not overlap with IRIS, we look location $x = 50$, $y = -113$ in Figure 5(b). This location shows that very few IRIS spectra exceed any of the parameter limits (Figure 15) and the movie shows that no spectra nearby in time or space are IRIS RBEs. However, examining the spectra by eye reveals several spectra which appear similar to spicule spectra, particularly those which pass the peak ratio requirement. For those which appear most spicule-like, the absorption and emission Doppler shifts both typically fall just short of the cutoff requirements. This suggests that with looser requirements, this analysis likely would detect an RBE at this location. It is important, however, to note that the majority of the spectra either display no spicule features at all, or display Doppler shifts in the redshifted direction. Even with looser limits, it is clear that IRIS and SST would not be in strong agreement.

This analysis identified three SST events for comparison with IRIS events, but a full understanding of spicule connections between Hα and Mg II will not be complete without additional study into the simultaneous behaviors of co-located Hα and Mg II spectra. The images in Figure 5 and in the associated video may appear to show definite co-temporal boundary differences between SST and IRIS spicules, but these must be treated with caution. Due to the time difference of up to 25 seconds between any two neighboring SST and IRIS pixels in these images and due to the fact that the SST data are derived from representative profiles and not directly from Hα spectra, additional analysis must be done to determine the exact spatial and temporal boundary relationships. To do so, the IRIS spectra must be directly compared with their co-aligned SST spectra and spatial, temporal, and spectral trends examined.

One of the primary assumptions in this method is that the Mg II line can be fit by the combination of a positive and a negative Gaussians. While this assumption holds true for most data, spectra with highly Doppler shifted or absent central inversions break this assumption. Because of this, fits for the most extreme spectra either have high χ^2 values or cannot be fit at all. When discarding poorly fitted spectra, the χ^2 cutoff is particularly important because the most extreme spicule spectra are most likely to have a poor fit. In the 2017 Plage dataset, a χ^2 of < 5 discards 44% of co-aligned spicule fits, a χ^2 of < 10 discards 16% of fits, and a $\chi^2 < 20$ discards 4% of fits. This analysis used a χ^2 of 10. Because this model struggles to fit the more extreme Doppler shifted spectra, we can assume that we are undercounting the number of extreme spicule events.

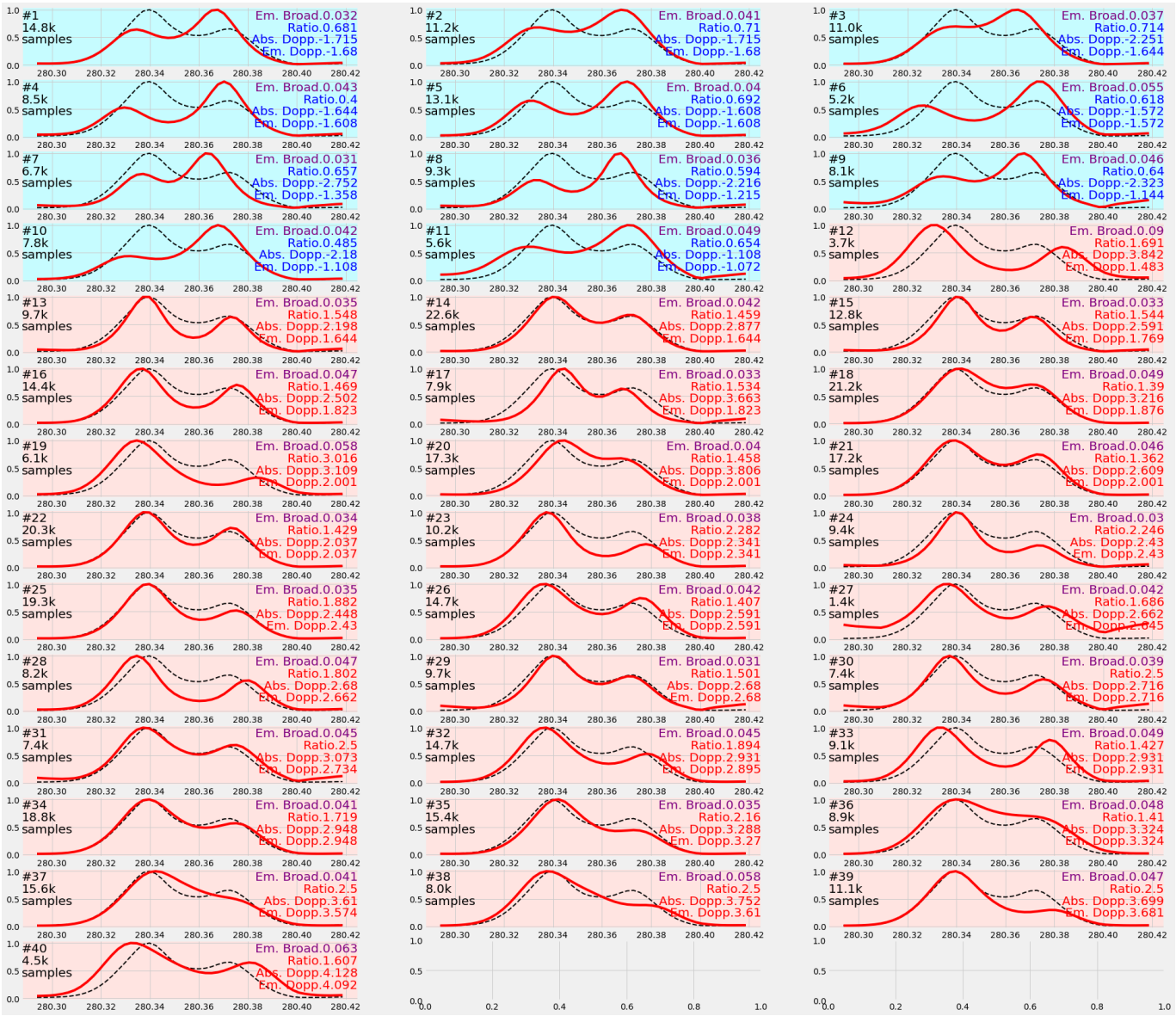

Figure 14. Spicule Representative Profiles, sorted by absorption Doppler shift. Solid red lines show each spectrum while dashed black lines provide a reference profile. Left of each spectrum is the profile number and how many samples contributed to that profile. To the right of each spectrum are the associated fitting parameters.

When examining the lambda-time plots of individual locations that feature the saw-tooth pattern shown in Figure 10 we note that while events are most often identified at the extremes of the saw-tooth pattern (which is indicative of Type I spicules), not all extremes are identified as events. While we do not assume that all extremes must be events, we did review the spectra at the extremes of the saw-tooth pattern to understand why they were not being identified. Most of these spectra observed either had a high χ^2, or failed to display both a broadening and a Doppler shift of the Gaussian emission feature. The lack of broadening and Doppler shift of the Gaussian emission feature may also be due to the extreme absorption of the Doppler-shifted plasma above, in the same way that one of the k2 peaks may be entirely suppressed.

5. CONCLUSION

Scientific research currently has a limited understanding of the middle and upper chromosphere compared to the lower chromosphere below it and the transition region and corona above it. This is due to the chromosphere's complex, dynamic, optically thick nature which makes it more complicated to model than coronal structures. Additionally the

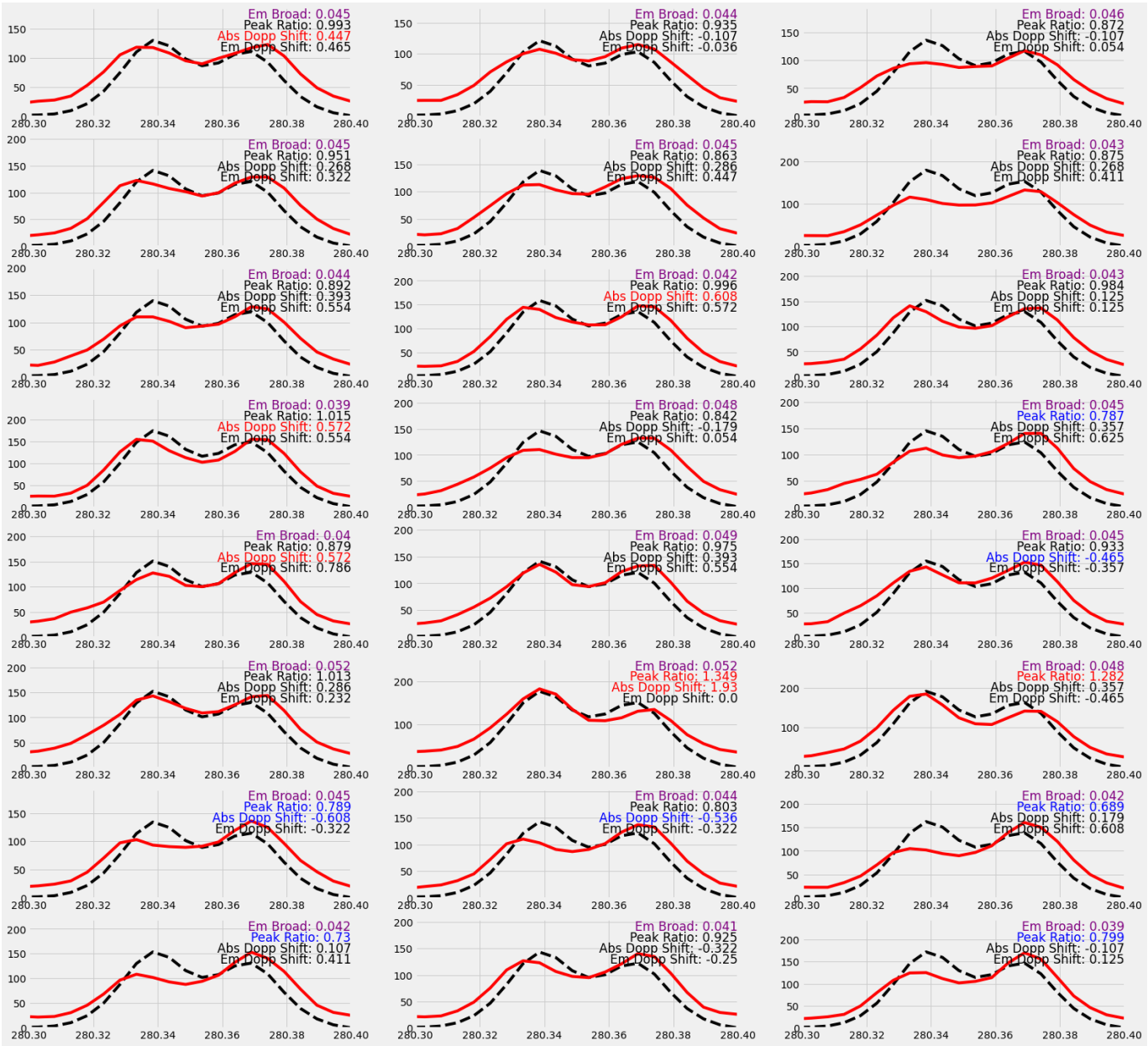

Figure 15. IRIS spectra which overlap with the SST RBE at $x = 50$, $y = -113$ in Figure 5(b). The figure is formatted similarly to Figure 9.

middle and upper chromosphere are only visible in EUV wavelengths such Mg II and Lyα which require space-based observations, compared to Hα ground-based observations of the lower chromosphere. Understanding this region is critical for several reasons. First, the chromosphere is the layer in the Sun's atmosphere where the environment changes from a plasma-dominated regime ($\beta > 1$ to a magnetically dominated regime ($\beta < 1$). This the specifics of this boundary are difficult to model, but critical to model correctly to understand predict the activities and risks of events such as CMEs, SEPs, and solar flares. Additionally, researchers still struggle to explain exactly how and why temperatures increase by a factor of 150 between the chromosphere and the corona. Ultimately the energy sources from the solar core, and so must necessarily pass through the chromosphere before reaching the transition region and corona. Additional research must be performed to understand exactly how energy is transferred between the lower chromosphere and the transition region.

This research built on the study by Herde et al. (2023) that showed spicules produce signatures in Mg II which result in changes to the absorption Doppler shift, emission Doppler shift, emission Gaussian width, and peak ratio of spectra, parameters which have been found by fitting the spectrum with a positive emission Gaussian plus a negative absorption Gaussian. This paper uses previously-identified spicules in co-observations to determine the exact cutoff values needed to identify these signatures. Because this process is entirely automated and requires no manual input, it can enable researchers to perform large-scale statistical studies similar to those already performed with lower-chromospheric Hα observations. This will assist in comparisons between the two regions and advance our understanding of spicule behavior as they fade from Hα observations.

We identify redshifted and blueshifted events in an active region at a rate of 0.039 arcsec^{-2} min^{-1} and 0.030 arcsec^{-2} min^{-1}. This is approximately 30% and 60% respectively lower than rates found by Bose et al. (2021b) while analyzing the same location. The coronal hole dataset yielded events at a higher rate. The decayed active network also yielded spicule identifications at a very high rate, but this rate is likely artificially inflated due to its limited Solar X spatial analysis. When considering fill factors, The decayed network displayed the lowest spicule fill factor, while the coronal hole dataset displayed the highest, closely followed by the Flare Watch and Plage datasets. We find event durations to be 76 s in a coronal hole, 38 s in a decayed network region, and 48 s in an active region. These values are all longer than the median duration of 27.2 s found by Bose et al. (2021b), which may be influenced by IRIS's lower temporal and spatial resolution than that study. Additionally both Type I and Type II spicules were identified in this in this analysis.

While this work shows exciting potential for upper chromospheric spicule identifications, it also displays some major limitations including spatial and temporal co-alignment and resolution differences between Hα and Mg II observations, differences due to analyzing k means cluster representative profile regions compared to direct spectral analysis, and known difficulties fitting and identifying the most extreme spicule spectra. Despite these difficulties, this work provides the first-ever tools to enable large-scale Mg II spicule analysis. It also provides the first statistical comparisons between Mg II and Hα so that researchers can begin to understand the differences between spicule activity in the lower chromosphere compared to the middle chromosphere.

Facilities: IRIS, SST(CRISP and CHROMIS), SDO(HMI)

Software: astropy (Astropy Collaboration et al. 2013, 2018, 2022), IRISpy

REFERENCES

Astropy Collaboration, Robitaille, T. P., Tollerud, E. J., et al. 2013, A&A, 558, A33, doi: 10.1051/0004-6361/201322068

Astropy Collaboration, Price-Whelan, A. M., Sipőcz, B. M., et al. 2018, AJ, 156, 123, doi: 10.3847/1538-3881/aabc4f

Astropy Collaboration, Price-Whelan, A. M., Lim, P. L., et al. 2022, ApJ, 935, 167, doi: 10.3847/1538-4357/ac7c74

Athay, R. G., & Holzer, T. E. 1982, The Astrophysical Journal, 255, 743, doi: 10.1086/159873

Bate, W., Jess, D., Nakariakov, V., et al. 2022, The Astrophysical Journal, 930, 129

Beckers, J. 1968, Solar Physics, 3, 367

Beckers, J. M. 1972, Annual Review of Astronomy and Astrophysics, vol. 10, p. 73, 10, 73

Bjørgen, J. P., Sukhorukov, A. V., Leenaarts, J., et al. 2018, Astronomy & Astrophysics, 611, A62

Bose, S., der Voort, L. R., Joshi, J., et al. 2021a, Astronomy & Astrophysics, 654, A51

Bose, S., Henriques, V. M., Joshi, J., & Rouppe van der Voort, L. 2019, Astronomy & Astrophysics, 631, L5

Bose, S., Joshi, J., Henriques, V. M., & Roupe van der Voort, L. 2021b, Astronomy & Astrophysics, 647, A147

Bose, S., Nóbrega-Siverio, D., De Pontieu, B., & Rouppe van der Voort, L. 2023, The Astrophysical Journal, 944, 171

Bose, S., Nóbrega-Siverio, D., De Pontieu, B., & Rouppe van der Voort, L. 2023, The Astrophysical Journal, 944, 171, doi: 10.3847/1538-4357/acb544

Chaurasiya, R., Bayanna, A. R., Louis, R., Pereira, T., & Mathew, S. 2024, The Astrophysical Journal, 970, 179

Chintzoglou, G., De Pontieu, B., Martínez-Sykora, J., et al. 2018, The Astrophysical Journal, 857, 73

—. 2021, The Astrophysical Journal, 906, 82

Cranmer, S. R., & Woolsey, L. N. 2015, The Astrophysical Journal, 812, 71

De Pontieu, B., Erdélyi, R., & James, S. P. 2004a, Nature, 430, 536

—. 2004b, Nature, 430, 536
De Pontieu, B., Hansteen, V., Rouppe van der Voort, L., van Noort, M., & Carlsson, M. 2007, The Astrophysical Journal, 655, 624
De Pontieu, B., Hansteen, V. H., Rouppe van der Voort, L., van Noort, M., & Carlsson, M. 2007, The Astrophysical Journal, 655, 624, doi: 10.1086/509070
De Pontieu, B., McIntosh, S. W., Hansteen, V. H., & Schrijver, C. J. 2009, The Astrophysical Journal, 701, L1
De Pontieu, B., McIntosh, S., Hansteen, V. H., et al. 2007, Publications of the Astronomical Society of Japan, 59, S655
De Pontieu, B., McIntosh, S., Carlsson, M., et al. 2011, Science, 331, 55
De Pontieu, B., Lemen, J., Kushner, G., et al. 2014a, Solar Physics, 289, 2733
De Pontieu, B., Title, A., Lemen, J., et al. 2014b, Solar Physics, 289, 2733
Ding, J., Madjarska, M., Doyle, J., et al. 2011, Astronomy & Astrophysics, 535, A95
Dover, F. M., Sharma, R., Korsós, M. B., & Erdélyi, R. 2020, The Astrophysical Journal, 905, 72
González-Avilés, J., Guzmán, F., Fedun, V., & Verth, G. 2020, The Astrophysical Journal, 897, 153
Hansteen, V. H., De Pontieu, B., Rouppe van der Voort, L., Van Noort, M., & Carlsson, M. 2006, The Astrophysical Journal, 647, L73
Henriques, V., Kuridze, D., Mathioudakis, M., & Keenan, F. 2016, The Astrophysical Journal, 820, 124
Herde, V. L., Chamberlin, P. C., Schmit, D., et al. 2023, The Astrophysical Journal, 946, 103
Iijima, H., & Yokoyama, T. 2017, The Astrophysical Journal, 848, 38
Ji, H., Cao, W., & Goode, P. R. 2012, The Astrophysical Journal Letters, 750, L25
Kuridze, D., Zaqarashvili, T., Henriques, V., et al. 2016, The Astrophysical Journal, 830, 133
Langangen, Ø., De Pontieu, B., Carlsson, M., et al. 2008, The Astrophysical Journal, 679, L167
Leenaarts, J., Pereira, T. M. D., Carlsson, M., Uitenbroek, H., & De Pontieu, B. 2013, The Astrophysical Journal, 772, 89
Lipartito, I., Judge, P. G., Reardon, K., & Cauzzi, G. 2014, The Astrophysical Journal, 785, 109
Martínez-Sykora, J., De Pontieu, B., Hansteen, V. H., et al. 2017, Science, 356, 1269
Matsumoto, T., & Shibata, K. 2010, The Astrophysical Journal, 710, 1857
Narang, N., Arbacher, R. T., Tian, H., et al. 2016, Solar Physics, 291, 1129
Nived, V., Scullion, E., Doyle, J., et al. 2022, Monthly Notices of the Royal Astronomical Society, 509, 5523
Pereira, T. D., De Pontieu, B., Carlsson, M., et al. 2014, The Astrophysical Journal Letters, 792, L15
Pereira, T. M., De Pontieu, B., & Carlsson, M. 2012, The Astrophysical Journal, 759, 18
Pereira, T. M., Rouppe van der Voort, L., & Carlsson, M. 2016, The Astrophysical Journal, 824, 65
Roberts, W. O. 1945, Astrophysical Journal, vol. 101, p. 136, 101, 136
Rouppe van der Voort, L., & de la Cruz Rodriguez, J. 2013, The Astrophysical Journal, 776, 56
Rouppe van der Voort, L., De Pontieu, B., Hansteen, V., Carlsson, M., & van Noort, M. 2007, The Astrophysical Journal, 660, L169
Rouppe van der Voort, L., De Pontieu, B., Pereira, T., Carlsson, M., & Hansteen, V. 2015, The Astrophysical Journal Letters, 799, L3
Rouppe van der Voort, L., Leenaarts, J., De Pontieu, B., Carlsson, M., & Vissers, G. 2009, The Astrophysical Journal, 705, 272
Rutten, R. J., Rouppe van der Voort, L. H., & De Pontieu, B. 2019, Astronomy & Astrophysics, 632, A96
Samanta, T., Tian, H., Yurchyshyn, V., et al. 2019, Science, 366, 890
Scharmer, G. B., Bjelksjo, K., Korhonen, T. K., Lindberg, B., & Petterson, B. 2003, in Innovative Telescopes and Instrumentation for Solar Astrophysics, Vol. 4853, SPIE, 341–350
Scharmer, G. B., Narayan, G., Hillberg, T., et al. 2008, The Astrophysical Journal, 689, L69
Schmit, D., Bryans, P., De Pontieu, B., et al. 2015, The Astrophysical Journal, 811, 127
Secchi, A. 1871, Anno 24, tomo 24
Sekse, D., Rouppe van der Voort, L., & De Pontieu, B. 2013a, The Astrophysical Journal, 764, 164
Sekse, D., Rouppe van der Voort, L., De Pontieu, B., & Scullion, E. 2013b, The Astrophysical Journal, 769, 44
Sekse, D. H., Rouppe van der Voort, L., & De Pontieu, B. 2012, The Astrophysical Journal, 752, 108
Shelyag, S., Litvinenko, Y., Fedun, V., et al. 2018, Astronomy & Astrophysics, 620, A159
Shetye, J., Doyle, J. G., Scullion, E., et al. 2016, Astronomy & Astrophysics, 589, A3
Skogsrud, H., Rouppe van der Voort, L., & De Pontieu, B. 2016, The Astrophysical Journal, 817, 124
Srivastava, A., Singh, B., Murawski, K., et al. 2023, The European Physical Journal Plus, 138, 209
Sterling, A. C., Harra, L. K., & Moore, R. L. 2010, The Astrophysical Journal, 722, 1644

Sterling, A. C., Moore, R. L., Samanta, T., & Yurchyshyn, V. 2020, The Astrophysical Journal Letters, 893, L45

Tian, H., DeLuca, E., Cranmer, S., et al. 2014, Science, 346, 1255711

Tsiropoula, G., Tziotziou, K., Kontogiannis, I., et al. 2012, Space science reviews, 169, 181

Tsuneta, S., Ichimoto, K., Katsukawa, Y., et al. 2008, Solar Physics, 249, 167

Vilangot Nhalil, N., Shetye, J., & Doyle, J. G. 2022, Monthly Notices of the Royal Astronomical Society, 515, 2672

Vourlidas, A., Beltran, S. T., Chintzoglou, G., et al. 2016, Journal of Astronomical Instrumentation, 5, 1640003

Yurchyshyn, V., Abramenko, V., & Goode, P. 2013, The Astrophysical Journal, 767, 17

Yurchyshyn, V., Abramenko, V., Kosovichev, A., & Goode, P. 2014, The Astrophysical Journal, 787, 58

Yurchyshyn, V., Cao, W., Abramenko, V., Yang, X., & Cho, K.-S. 2020, The Astrophysical Journal Letters, 891, L21